



Efficient photodechlorination of chlorophenols on polarized $M\text{ZnB}_5\text{O}_{10}$ ($M = \text{Na}$ and K) nonlinear optical materials



Jing Liu^{a,b}, Xiaoyun Fan^{b,*}, Yunqing Zhu^b, Jie Zhao^b, Fengxing Jiang^a, Shuai Chen^b, Hui Sun^a, Jingkun Xu^{a,*}, Wenye Deng^b, Chuanyi Wang^{b,*}

^a Department of Physics, Jiangxi Science and Technology Normal University, Nanchang 330013, China

^b Laboratory of Environmental Sciences and Technology, Xinjiang Technical Institute of Physics & Chemistry, and Key Laboratory of Functional Materials and Devices for Special Environments, Chinese Academy of Sciences, Urumqi 830011, China

ARTICLE INFO

Article history:

Received 15 May 2015

Received in revised form 15 July 2015

Accepted 19 July 2015

Available online 26 July 2015

Keywords:

Borate-based photocatalyst

Dechlorination

Polarization

Surface potential

ABSTRACT

Charge separation is crucial for increasing the activity of semiconductor-based photocatalysts. In this work, a series of non-centric structure materials: $\text{K}_3\text{ZnB}_5\text{O}_{10}$ (KZBO), $\text{K}_2\text{NaZnB}_5\text{O}_{10}$ (KNZBO) and $\text{Na}_3\text{ZnB}_5\text{O}_{10}$ (NZBO), called nonlinear optical materials, show high activity in the chlorophenols dechlorination under UV-vis light irradiation ($\lambda > 254$ nm). The obtained dechlorination efficiency is one order of magnitude higher than that of commercial $\text{P}_2\text{O}_5\text{TiO}_2$ catalyst under same reaction conditions. Such materials possess a spontaneous polarization arising from the displacement of the center of the positive and negative charges, providing a driving force for the separation of photogenerated electrons and holes and thereby mitigating the effect of charge recombination as confirmed by Kelvin probe force microscopy. The present work implies that the nonlinear optical materials hold promise in degradation of organic chlorinated pollutants.

© 2015 Elsevier B.V. All rights reserved.

1. Introduction

Chlorophenols (CPs) are widely present in industrious waste water of paper, dyes, pesticides, textiles, and petrochemicals [1]. Most CPs are extremely difficult to be degraded due to their stability due of the chlorine–carbon bonds [2]. Significant efforts have been devoted toward removing the pollutants via biological treatments [3], physical methods [4], and catalytic oxidation [5]. However, these methods are limited by the toxicity of CPs to microbes or merely transfer the pollutants with the risk of secondary contamination. Photocatalysis is regarded as an effective way to dechlorination of CPs due to its harmless, low cost, high chemical stability and high efficiency [6,7]. In the past four decades, there have been over 50 semiconductor systems and some novel materials investigated in an effort to find a suitable and efficient photocatalyst, such as, TiO_2 [8], CdS [9], carbon nitrides ($\text{g-C}_3\text{N}_4$) [10], Ag_3PO_4 [11], graphene-based [12], and so on. However, photocatalysis efficiency is often limited due to the high rate of recombination between photoexcited electrons and holes [13].

One effective approach to mitigate recombination of charge carriers is to adopt internal electric fields, which provide a driving force for the separation of photogenerated electrons and holes [14]. Internal electric fields can arise from ferroelectric phenomena [15,16], p-n junctions [17,18], polar surface terminations [19,20], and polymorph junctions [21]. Ferroelectric materials possess spontaneous polarization arising from the displacement of the center of the positive and negative charges which can induce the accumulation of charges at the surfaces [22]. The spontaneous polarization with directions pointing from the bulk to the surface will produce a positive charge on the surface (C^+ domain), and the polarization pointing away from the surface to the bulk will generate a negative charge (C^- domain) [23]. The internal depolarization field will drive free electrons to the surface of a C^+ domain. This charge redistribution creates an electric field in the space charge region [23]. In this case, the photogenerated electrons can easily reach the surface and give rise to oxidation and reduction products at different locations. Among the borate materials, $\text{K}_3\text{B}_6\text{O}_{10}\text{Br}$ has been reported to show high dechlorination efficiency, implying that borates materials hold great potential in the field of photocatalysis for practical application [24].

Metal oxides with d^{10} configuration are active for water decomposition suggesting the possibility of establishing a new photocatalyst group with different electronic structures [25]. The polar displacement of $d^{10}\text{Zn}^{2+}$ ion is capable of forming the non-centric

* Corresponding authors.

E-mail addresses: xyfan@ms.xjb.ac.cn (X. Fan), xujingkun@tsinghua.org.cn (J. Xu), cywan@ms.xjb.ac.cn (C. Wang).

structure [26] which can facilitatively produce an internal electric field. In addition, the alkaline metal atoms in borate motifs have a great effect on the crystal structure and light absorption. The distorted structures of alkaline metal–oxygen ($M-O_n$) polyhedron are proposed to be responsible for efficient photoexcitation and charge separation, which directly enhances the photocatalytic performance [27]. From this prospect, it is of importance to perform extensive research on for the photocatalytic properties of the complexes with the d^{10} configuration and alkaline metals in borate motifs.

Herein, we demonstrate that stable and inexpensive $M_2O-ZnO-B_2O_3$ (M = alkali metal atoms) alkali borate crystals with non-centric structure (KZBO, KNZBO, and NZBO), which are generally reported as nonlinear optical materials [28–30], can also function as efficient UV-vis light-responsive photocatalysts for CPs dechlorination. The catalysts exhibit high efficiency in dechlorination of 2-chlorophenol (2-CP), 4-chlorophenol (4-CP), 2,4-DCP, and 2,4,6-trichlorophenol (2,4,6-TCP) under UV-vis light irradiation ($\lambda > 254$ nm). Using 2,4-DCP as an example, approximately 83%, 75%, and 68% of the total chloride content was converted into Cl^- anions after 10 min of illumination at – KZBO, KNZBO and NZBO, respectively. The different activities for CPs dechlorination by the three catalysts are closely related to the substitution of M^+ cations, which have different radius playing a significant role in the polarization property of MZBO. To the best of our knowledge, this is the first time to report the novel MZBO crystal materials as photocatalysts for dechlorination reactions.

2. Experimental

2.1. Materials

Chemicals were purchased from Tianjin Chemicals, Inc., including K_2CO_3 , Na_2CO_3 , ZnO , Na_2SO_4 , $Na_2B_4O_7 \cdot 10H_2O$, and H_3BO_3 . 2-CP, 4-CP, 2,4-DCP and 2,4,6-TCP and $C_6H_{11}NO$ (DMPO) were purchased from Sigma–Aldrich. Deionized water was used throughout this study.

2.2. Catalysts preparation

The sample compounds were prepared by traditional solid-state reaction techniques. All reagents were analytical grade. For the preparation of KZBO crystals, a stoichiometric mixture of K_2CO_3 , ZnO and H_3BO_3 was ground in an agate mortar and packed into crucible, the raw materials were heated to 400 °C, held for 12 h and at 600 °C for 48 h. Under the same condition, a stoichiometric mixture of K_2CO_3 , $Na_2B_4O_7 \cdot 10H_2O$, ZnO , H_3BO_3 , and ZnO , Na_2CO_3 and H_3BO_3 were prepared for the synthesis of KNZBO and NZBO powders.

2.3. Characterization

X-ray diffraction (XRD) patterns of the samples were recorded on a Bruker D8 Advance X-ray diffractometer equipped with a diffracted-beam monochromator set for $Cu K\alpha$ radiation ($\lambda = 1.5418 \text{ \AA}$). The diffuse reflectance absorption spectra (DRS) of the samples were recorded in the range from 200 to 800 nm on a Solidspec-3700 DUV spectrometer and using $BaSO_4$ as a reference. The morphologies of samples were observed on a scanning electron microscope (SEM) using a ZEISS SUPRA55VP apparatus and energy dispersive X-ray (EDX) spectroscopic analysis was conducted by EDX8000. High performance liquid chromatography (HPLC) (Ultimate 3000, Dionex) was carried out with a C18 column (4.6 mm × 250 mm). A mixture of methanol and water [85/15 (v/v)] was used as an effluent, and the flow rate was 0.5 mL/min.

The intermediate products during 2,4-DCP degradation were qualitatively analyzed by a liquid chromatography–mass spectrometry (LC–MS, Agilent 1290). The size of the sample loop was 20 mL. The wavelength of the detector was set at 282 nm. Ion chromatography (IC) was measured by the ICS 5000. The UV-vis absorption spectral analysis was performed on the spectrometer UV-1800. The Brunauer–Emmett–Teller (BET) surface area was obtained from the N_2 adsorption/desorption isotherms recorded at 77 K (QUADRA-SORB IQ, Quantachrome Instrument Corp.).

The photocurrents of UV light on and off studies were measured on a CHI660E electrochemical system using a standard three-electrode cell with a working electrode (10 mm × 10 mm), a platinum plate as the counter electrode, and a standard calomel electrode (SCE) as the reference electrode. The MZBO film was prepared on an ITO glass, followed by air-drying. The experiments were performed in a 50 mL quartz cylinder reactor which was placed in front of a 500 W mercury lamp ($\lambda > 254$ nm; Perfect Light Company, Beijing, China). The intensity of light at the catalyst film was 245 mW/cm². The photocurrents of UV light on and off were measured at 0.05 V. The photoelectron chemical (PEC) activities of the samples were all evaluated by the removal of 2,4-DCP (with an initial concentration of 50 mg/L) in a 0.1 M Na_2SO_4 solution.

Atomic force microscopy (AFM) combined with Kelvin probe force microscopy (KPFM) measurements were performed at room temperature with an atomic force microscope (Bruker Multimode 8). In KPFM, electrostatic forces between the tip and sample result from a non-contact potential difference. The non-contact potential difference is instantly and automatically nullified by a DC bias (≈ 1570 mV) applied to the probe tip. This DC bias is recorded at each position to generate a potential image. Topography was measured using tapping mode at the resonance frequency (75 kHz) of the conductive Pt/Ir coated AFM tip (2.8 N/m). In the experiment, MZBO nanoparticles were first dispersed in water and then sprayed on a Pt substrate to form a film. The sample was baked in a dry oven at 400 °C for 6 h. For the light irradiation experiment, a mercury lamp ($\lambda > 254$ nm) and a convex lens with a focusing spot size (d) of 1.5 cm were used to introduce focused UV light onto the measurement region between the tip of the atomic force microscope and sample.

Hydroxyl radicals were determined by a DMPO spin-trapping EPR method at room temperature on a Bruker E500 spectrometer. Experiment was performed with a capillary Pyrex glass tube under fixed conditions (5 g/L catalyst, and 25 g/L DMPO), and the EPR spectra were recorded after irradiation for 3 min by the Mercury lamp.

2.4. Photocatalysis

Photocatalytic activity tests for all samples were conducted at room temperature. During the experiment, 50 mg of a tested photocatalyst sample was dispersed in 100 mL solution of CPs (2-CP (20 mg/L), 4-CP (20 mg/L), 2,4-DCP (50 mg/L), and 2,4,6-TCP (50 mg/L) in a 250 mL glass beaker and stored for 20 min while being stirred in the dark to attain adsorption equilibrium. The reactor was then illuminated by a 500 W mercury light ($\lambda > 254$ nm). The intensity of the light on sample system was measured to be 254 mW/cm² by using a spectroradiometer. Samples were withdrawn periodically from the reactor. The percentage of residual CP solution at a selected time of irradiation is given by C/C_0 , where C_0 is the concentration of the CP solution at the initial stage, and C is the concentration at selected irradiation times (0, 2, 4, 6, 8, and 10 min). For comparison, blank experiments were conducted under the same condition. The concentration of each chlorophenol was measured using high-performance liquid chromatography.

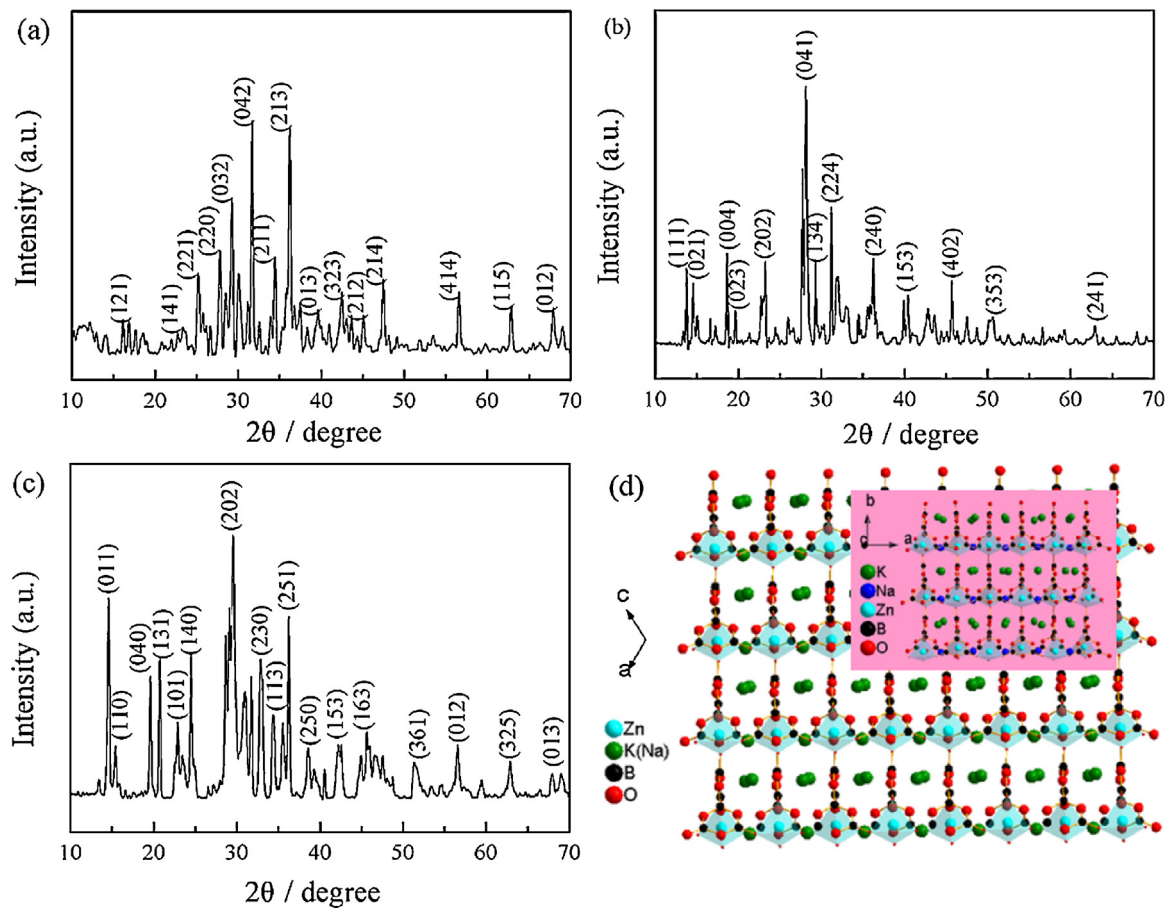


Fig. 1. XRD pattern of (a) KZBO, (b) KNZBO, (c) NZBO samples and (d) schematic drawing of the crystal unit.

3. Results and discussion

3.1. Structure and morphology of samples

The crystal structures of KZBO, KNZBO, and NZBO belong to the monoclinic space group $P21/n$, $C2/c$, and $P21/n$ [28–30] as confirmed by XRD analysis (Fig. 1). The basic structural unit is a double ring $[B_5O_{10}]$ consisting of one $[BO_4]$ tetrahedron and four $[BO_3]$ triangles. Each $[B_5O_{10}]$ group is linked to four different $[ZnO_4]$ tetrahedra through its terminal O atoms and likewise each $[ZnO_4]$ tetrahedron shares its four vertices with four neighboring $[B_5O_{10}]$ groups to form a two-dimensional (2D) infinite $[ZnB_5O_{10}]$ layer (Fig. S1). K

and Na metal cations between these layers assist coupling the layers together by enjoying O atoms to generate a three-dimensional network. The purity of the samples was also determined by EDS measurement (Fig. S2). The presence of elements and atomic percentages confirm that the as-prepared samples are of MZBO. The as-prepared samples are sheet and bulk in shape as observed in the SEM images (Fig. S2).

3.2. Optical absorption

Fig. 2(a) depicts the UV-vis absorption spectra of MZBO samples. As shown in Fig. 2(a), all three MZBO samples possess a 410 nm

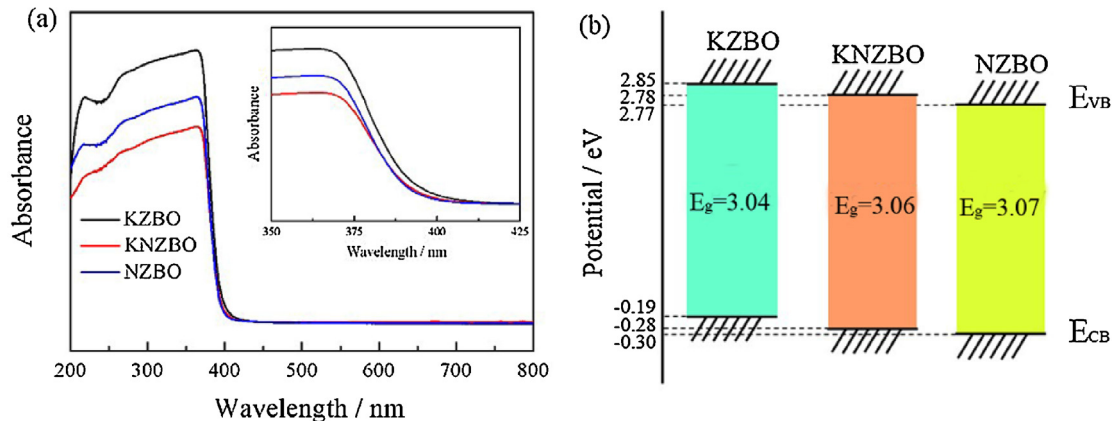


Fig. 2. (a) UV-vis diffusive reflectance spectrum and (b) the band structure of MZBO samples.

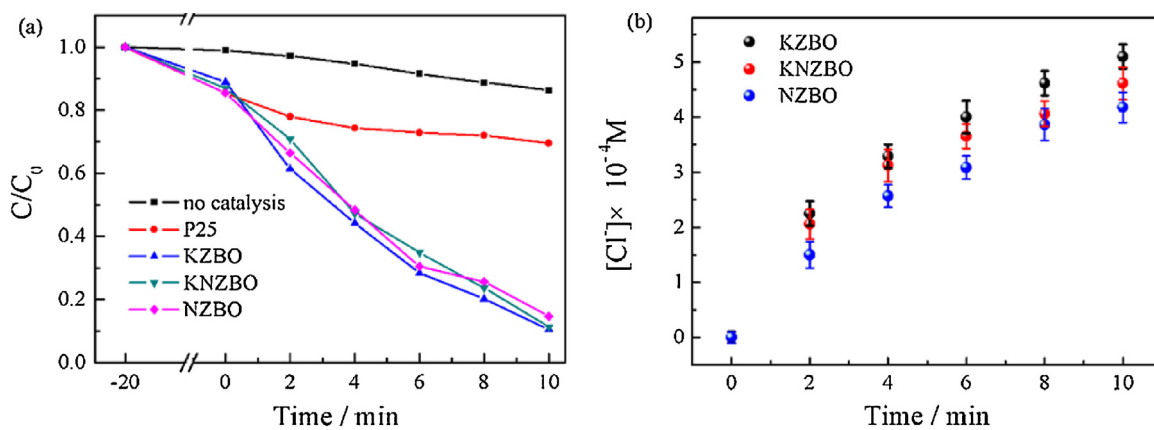


Fig. 3. (a) Photodechlorination of 2,4-DCP in aqueous dispersions under UV-vis light irradiation. (b) Formation of Cl^- during the photodechlorination process.

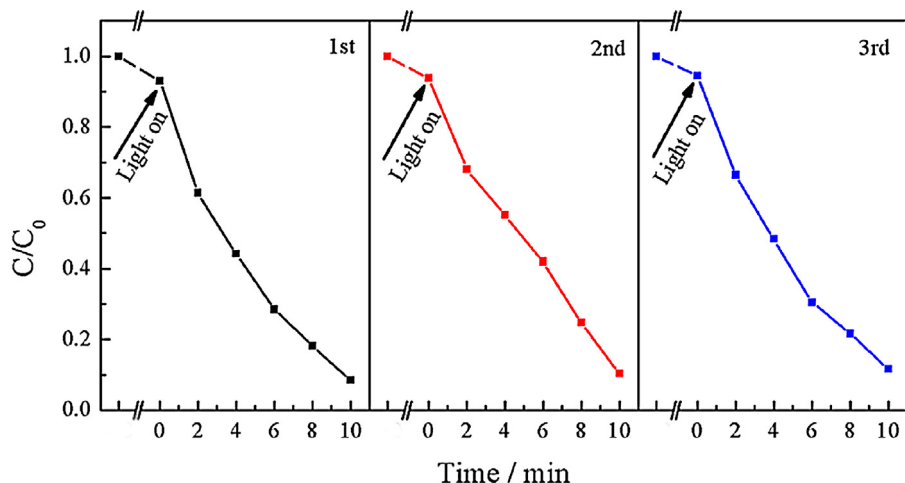


Fig. 4. Repeated experiments for the decomposition of 2,4-DCP by KZBO powder under UV-vis light irradiation.

absorption band-edge in the UV region. Theoretical band structure of MZBO is constructed to predict the band positions by the following Eqs. (1) and (2), respectively [31]:

$$E_{VB} = X - E_e + 0.5E_g \quad (1)$$

$$E_{CB} = E_{VB} - E_g \quad (2)$$

where X is the electronegativity of semiconductor, which is the geometric mean of the electronegativity of constituent atoms ($X_K = 2.7882$ eV, $X_{Na} = 2.5378$ eV, $X_{Zn} = 3.7515$ eV, $X_O = 8.3703$ eV, $X_B = 4.5851$ eV) [32]. E_g is the band gap energy of semiconductor; E_{VB} is valence band (VB) edge potential; E_{CB} is conduction band (CB) edge potential; E_e is the energy of free electrons on hydrogen scale (4.5 eV). The band structures of MZBO are shown in Fig. 2(b). It is definite that the alkali metal atoms substitution influences the optical properties of the crystal.

3.3. Photocatalytic activity

The photocatalytic activity of MZBO was tested by measuring the dechlorination of CPs under UV-vis and visible light irradiation. As shown in Fig. 3(a), the concentration of 2,4-DCP almost decreases to zero within 10 min. The conversion of the chloride to Cl^- anions is 83% for KZBO, 75% for KNZBO and 68% for NZBO, respectively (Fig. 3(b)). To confirm the photocatalytic process, blank tests were performed. No obvious degradation of 2,4-DCP is observed in the absence of photocatalysts, supporting the considerable photocatalytic activity of MZBO. The photocatalytic activity

was further tested under the light equipped with an ultraviolet cut-off filter (≥ 400 nm). As a result, the 2,4-DCP was hardly degraded within 50 min (Fig. S3), indicating that the photoactivity of MZBO is consistent with their spectral response that they can only absorb photons in wavelength shorter than 410 nm. The stability of MZBO was also studied. After three cycles of degradation of 2,4-DCP,

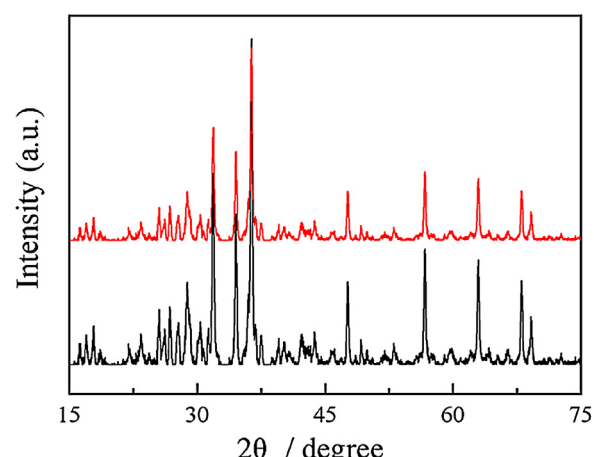


Fig. 5. XRD pattern of KZBO before (black line) and after three cycles (red line) in degradation of 2,4-DCP under UV-vis light irradiation. (For interpretation of the references to color in figure legend, the reader is referred to the web version of the article.)

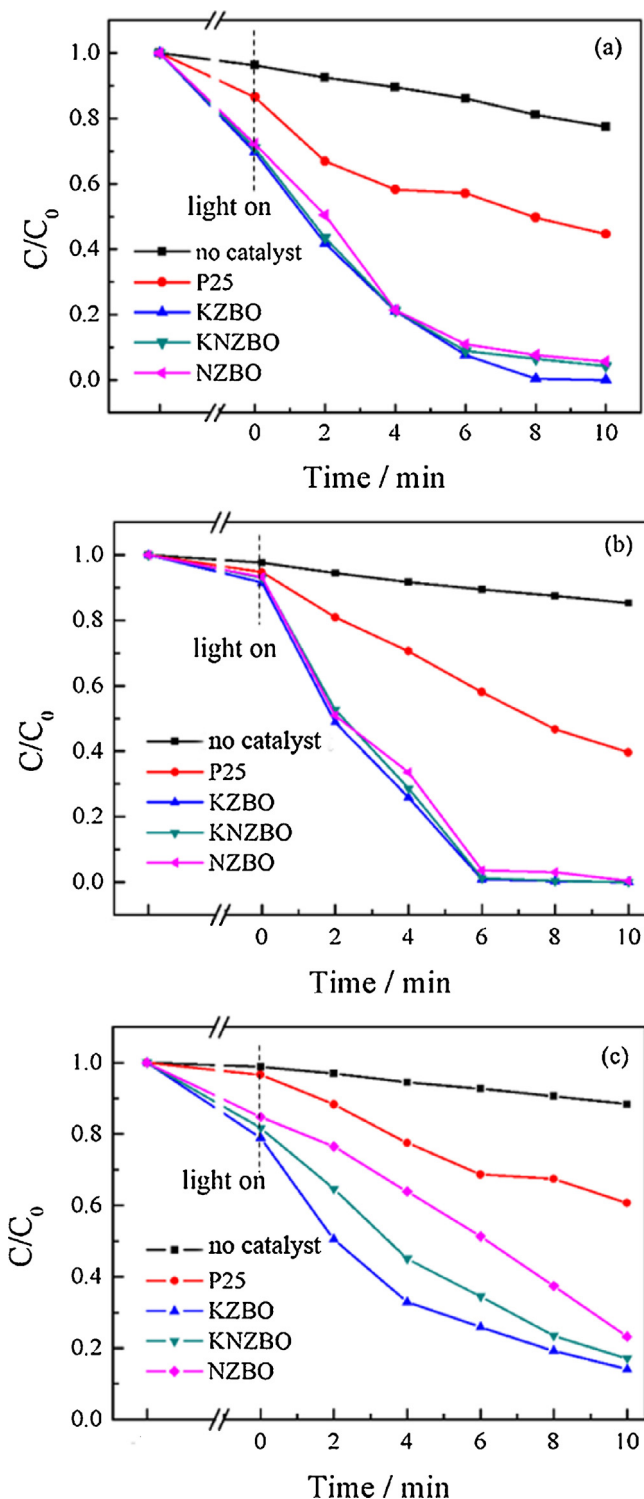


Fig. 6. Photodechlorination of (a) 2-CP, (b) 4-CP, (c) 2,4,6-TCP in aqueous dispersions under UV-vis light irradiation.

the dechlorination efficiency of KZBO, KNZBO and NZBO almost maintains the same level as the original one and shows a negligible reduction by about 0.18%, 0.77% and 1.51%, respectively (Fig. 4 and Fig. S4). Furthermore, no obvious difference is observed in the XRD patterns before and after the dechlorination reaction (Fig. 5 and Fig. S5), further indicating the stability of the MZBO samples. Altogether, the three samples show good stability with the order

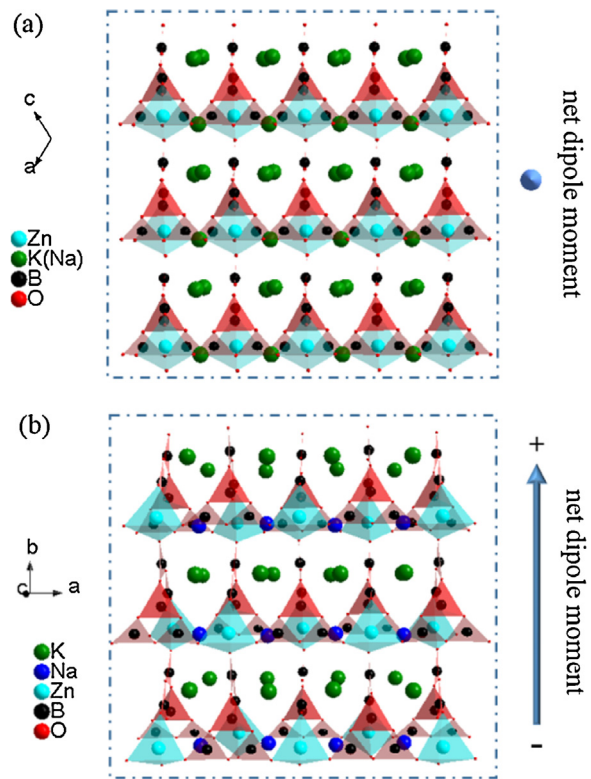


Fig. 7. Ball-and-stick diagram of the MZBO structure, and an electric polarization along the *b*-axis direction as shown by the blue arrows. (For interpretation of the references to color in figure legend, the reader is referred to the web version of the article.)

$KZBO \geq KNZBO \geq NZBO$. The photodechlorination reactions performed on other CPs (2-CP, 4-CP, and 2,4,6-TCP) are shown in Fig. 6.

The dechlorination of CPs by UV-vis light in the presence of MZBO follows pseudo-first-order process:

$$\frac{d[C]}{dt} = -k[C] \quad (3)$$

where k is the pseudo-first-order rate constant (min^{-1}), t is the reaction time, and $[C]$ is the aqueous phase concentration of CPs. The k can be determined from the linear relationship of $\ln([C]_t/[C]_0)$ versus time. In terms of 2,4-DCP, the rate constant for photodechlorination at KZBO, KNZBO, and NZBO was 0.2067 min^{-1} , 0.1971 min^{-1} , 0.1734 min^{-1} , respectively, almost 10 times higher than that of the commercial P25 TiO_2 catalyst (0.0184 min^{-1}), clearly illustrating the excellent photocatalytic activity of MZBO toward CPs dechlorination. The degradation performance of P25 and MZBO photocatalytic systems has been systematically compared (Table 1).

3.4. Internal electric field

Surface area often plays an important role in catalytic reactions. However, the high photocatalytic activity of MZBO in this work is not due to the effect by surface area, as the BET surface areas for three samples KZBO, KNZBO and NZBO are not big; they are $0.951 \text{ m}^2/\text{g}$, $0.806 \text{ m}^2/\text{g}$, and $0.661 \text{ m}^2/\text{g}$, respectively, according to the nitrogen absorption-desorption isotherm measurements (Fig. S6). To examine the probable cause for the high photocatalytic activity, the bond dipole moments of the system were investigated based on the bond-valence model [33]. A complete calculation of dipole moments for the constituted polyhedra is listed in Table 2. The trigonal $[\text{BO}_3]$ and tetrahedral $[\text{BO}_4]$ in KZBO, KNZBO, and NZBO give slightly different dipole moment values. However, the

Table 1The rate constants (k) for dechlorination of CPs by MZBO and P25 samples.

		Blank	P25	KZBO	KNZBO	NZBO
2-CP	k (min ⁻¹)	0.0216	0.0603	0.8949	0.4803	0.3719
	r^2	0.9977	0.9642	0.9980	0.9968	0.9894
4-CP	k (min ⁻¹)	0.0133	0.0887	0.9517	0.8594	0.5273
	r^2	0.9927	0.9935	0.9916	0.9679	0.9717
2,4-DCP	k (min ⁻¹)	0.0140	0.0184	0.2067	0.1971	0.1734
	r^2	0.9903	0.9858	0.9838	0.9800	0.9700
2,4,6-TCP	k (min ⁻¹)	0.0112	0.0165	0.1680	0.1608	0.1304
	r^2	0.9977	0.9866	0.9884	0.9969	0.9925

Table 2Dipole Moments of BO_n ($n = 3, 4$), and ZnO_4 polyhedra in MZBO crystals.

KZBO		KNZBO		NZBO	
Polyhedral unit	Dipole moment/debye	Polyhedral unit	Dipole moment/debye	Polyhedral unit	Dipole moment/debye
ZnO_4	1.7054	ZnO_4	1.2807	ZnO_4	1.2479
$B(1)O_3$	0.9419	$B(1)O_3$	0.9042	$B(1)O_3$	1.0164
$B(2)O_4$	0.2842	$B(2)O_3$	0.8068	$B(2)O_3$	0.8106
$B(3)O_3$	0.9675	$B(3)O_4$	0.3371	$B(3)O_4$	0.2276
$B(4)O_3$	0.9157	$B(4)O_3$	0.8620	$B(4)O_3$	0.7903
$B(5)O_3$	0.5512	$B(5)O_3$	0.8592	$B(5)O_3$	1.0008

tetrahedral $[ZnO_4]$ has a dominantly different value in three samples. It is also well-established that large cations are prone to be polarized, which influences the cation's surrounding environment and likely affects the electronic structure [34]. With the increase in the atomic radius of the M^+ cation ($M = K$ or Na), in KZBO, KNZBO, and NZBO, the cation's contribution to the electronic structure becomes more important. The net dipole moment of the tetrahedral $[ZnO_4]$ has a large negative charge that maintains a large dipole moment. Overall, the dipole moment for the three materials

in the order KZBO > KNZBO > NZBO. Thus, MZBO can be easily polarized (Fig. 7), causing a highly inductive effect therein [35].

To demonstrate the intricate relationship between the structure and photocatalytic function, we investigated photoinduced charge transfer properties of the MZBO by means of KPFM, which is a tool that enables nanometer-scale imaging of the surface potential on a broad range of materials [36]. Taking the KZBO as an example, the morphology determined by AFM does not show apparent change before and after irradiation (Fig. 8(a) and (c)). However, the surface

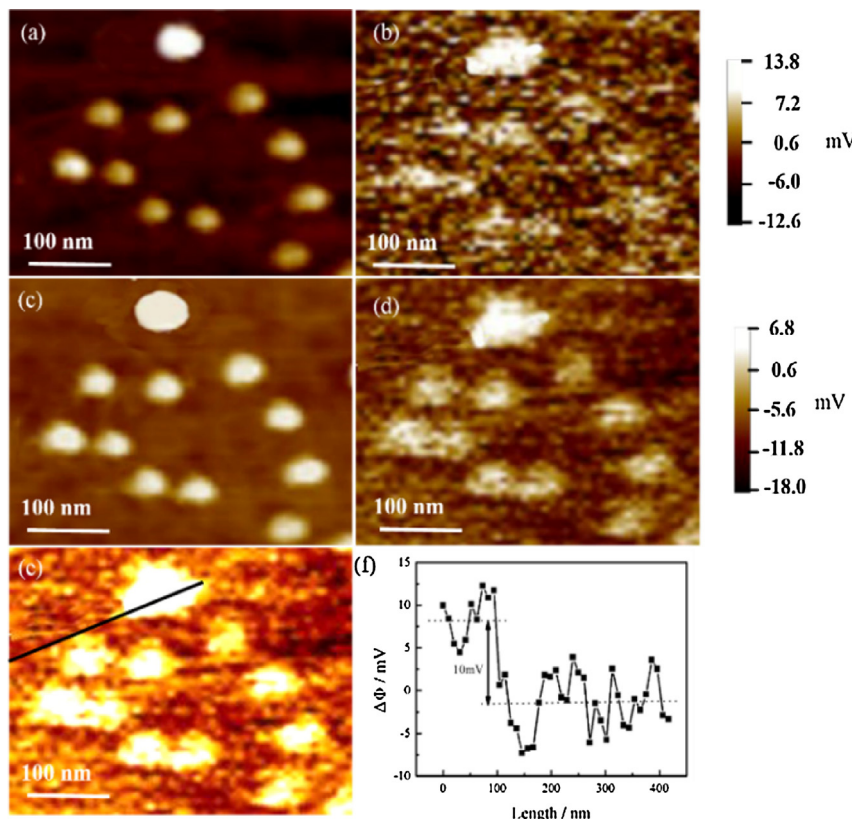


Fig. 8. AFM imaging and surface potential analysis for KZBO: topographic images before (a) and after (c) light irradiation, and corresponding surface potential images before (b) and after (d) light irradiation; (e) Differential image obtained by subtracting panel d from panel b; (f) Surface potential profile along the black line in panel e.

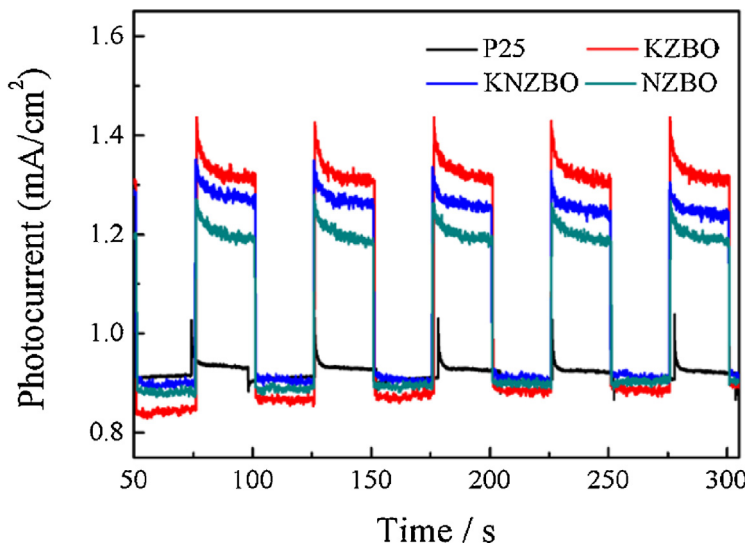


Fig. 9. Photocurrent spectra of the MZBO samples and P25.

potential of the whole scanned region is drastically decreased after UV-vis light irradiation (Fig. 8(b) and (d)). In order to quantitatively determine surface potential differences, a differential surface potential image is obtained by subtracting panel d from panel b (Fig. 8(e)). As shown in Fig. 8(f), the surface potential difference is deduced to be ~ 10 mV. The difference is attributed to the light response for different domains of the material, and after light irradiation the charge separation is driven by the internal electric fields. This result provides direct evidence that the presence of the internal field provides a driving force for the separation of photogenerated electrons and holes leading to high photoactivity [37].

The PEC measurements of the MZBO, which directly correlates with the recombination efficiency of the photogenerated carriers [38,39], further confirm that the photon-to-electron conversion efficiency is affected by the non-centric structure. Fig. 9 shows the transient photocurrent responses via several on-off cycles of MZBO and P25 electrodes under UV-vis light irradiation. The anodic photocurrent of MZBO is obviously higher than that of P25 TiO_2 . The higher photocurrent of MZBO in transient photocurrent response suggests a lower rate of recombination of electrons and holes during photoreaction. Therefore, MZBO samples have an effective separation of photogenerated electron–hole pairs resulting in fast interfacial charge transfer.

As discussed above, MZBO has fast interfacial charge transfer resulting from an effective separation of photogenerated electron–hole pairs. The transfer of photogenerated carriers in MZBO materials is affected by the dipolar field. The internal dipolar field within MZBO creates charged surfaces that cause photogenerated carriers to move into opposite directions. As shown in Fig. 10, in a unit cell, along the polarization vector direction, electrons flow toward the surface to cause the reduction reaction. The photogenerated holes cause the oxidation reaction in the opposite direction. Under these conditions, highly efficient separation of the photogenerated electron–hole pairs is achieved in the MZBO materials.

3.5. Mechanism for 2,4-DCP photodechlorination

A mechanism for 2,4-DCP degradation is proposed based on the intermediates and end products identified by LC-MS analysis (Fig. S7 and Table S1). As shown in Fig. 11, the $\cdot\text{OH}$ can attack 2,4-DCP at the positions of the Cl atom to replace the electron-withdrawing Cl atoms, converting 2,4-DCP first to chlorocatechol and then to

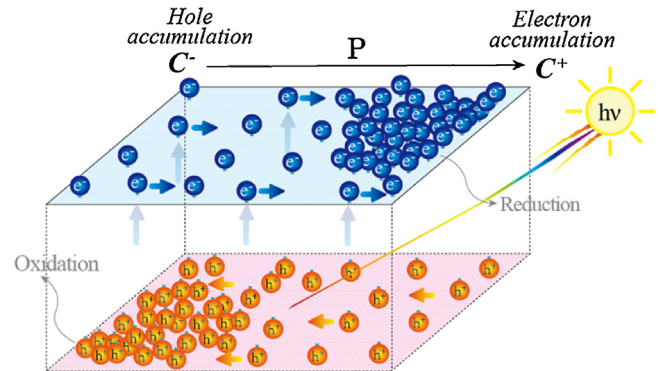


Fig. 10. Schematic illustration of a non-centric structured MZBO photocatalyst.

1,4-benzoquinone. In addition, 2,4-DCP can also undergo reductive dechlorination to generate 4-chlorophenol first and then reacts with hydroxyl radicals, leading to the formation of catechol and phenol. Although the 2,4-DCP cannot be completely degraded by KZBO, the end products are less toxic than that of 2,4-DCP and can be biodegraded into harmless compounds by microorganisms under both aerobic and anaerobic conditions [40]. The formation of $\cdot\text{OH}$ was detected by EPR spin-trapping technique using a spin-trapping agent-DMPO to further explore the photodechlorination pathway. Fig. 12 shows the change in the EPR intensity of free radicals produced from the UV-vis illumination for 3 min of aqueous solution containing MZBO in the presence of DMPO. A quartet of signals with relative intensities of 1:2:2:1 from the DMPO-OH adducts were detected during the reaction process, suggesting that hydroxyl radicals were formed in the catalytic reaction [41]. Moreover, the signal intensity of free radicals is increased obviously in the order KZBO > KNZBO > NZBO, which further confirms the largest polarization of the KZBO could efficiently enhance the reaction rate compared to KNZBO and NZBO samples. In general, the dechlorination processes of 2,4-DCP at KZBO are proposed in Eqs. (4)–(9):



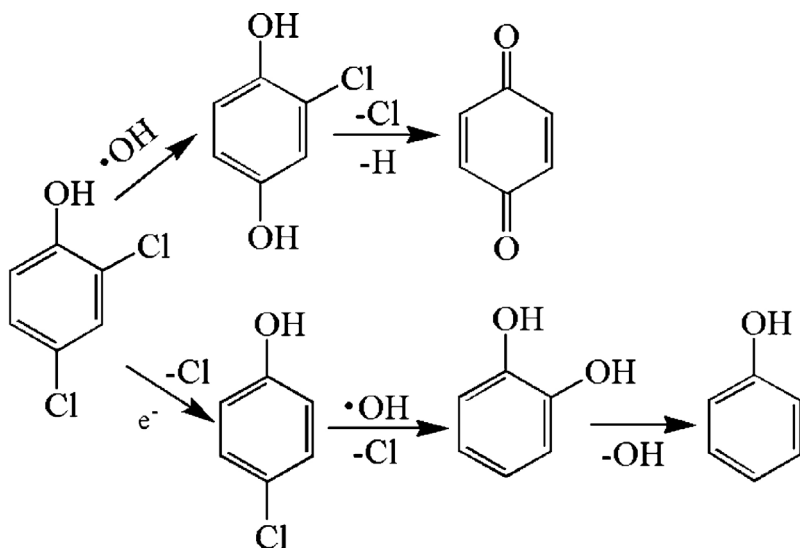


Fig. 11. The reaction pathway for 2,4-DCP photodechlorination by KMBO.

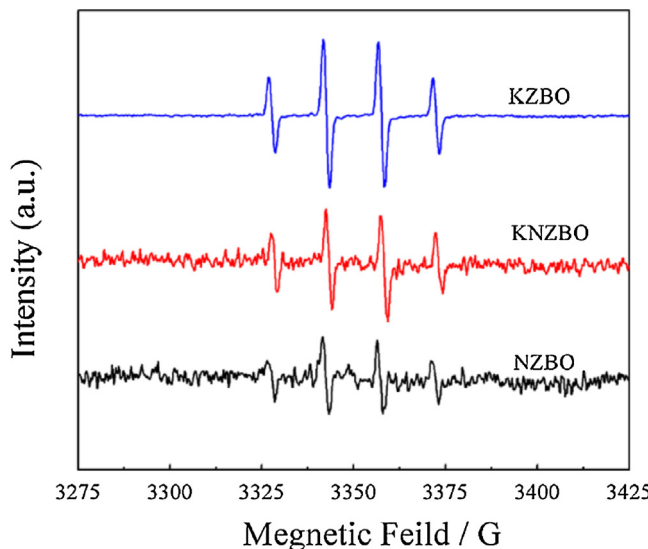
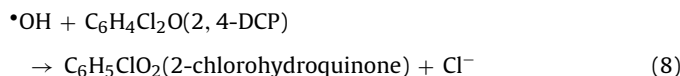


Fig. 12. DMPO spin-trapping EPR spectra in the presence of 5 g/L catalyst and 25 g/L DMPO after 3 min irradiation by the UV-vis light irradiation.



4. Conclusions

In conclusion, nonlinear optical materials, $\text{K}_3\text{ZnB}_5\text{O}_{10}$ (KZBO), $\text{K}_2\text{NaZnB}_5\text{O}_{10}$ (KNZBO) and $\text{Na}_3\text{ZnB}_5\text{O}_{10}$ (NZBO), prepared by traditional solid-state routes show high photocatalytic activity in dechlorination of CPs under UV-vis light irradiation ($\lambda > 254 \text{ nm}$). The high polarizability of MZBO induces the internal electric fields at the space-charge regions, which facilitates the charge separation of photogenerated electron–hole pairs and thus enhances the photocatalytic activity. The M^+ cations with different radius play a significant role in the photocatalytic properties of MZBO, as large cations are prone to be polarized, which influences the cation's surrounding environment. The largest K^+ radius of KZBO is responsible

for the largest polarization ability and highest dechlorination efficiency among the three sample catalysts. A possible reaction pathway for 2,4-DCP dechlorination by KZBO upon UV-vis light irradiation is proposed. Hydrodechlorination was found to be the major reaction pathway for 2,4-DCP dechlorination which could react with hydroxyl radicals to produce 1,4-benzoquinone. The findings are expected to open up a new window toward the design of highly efficient photocatalysts using nonlinear optical materials.

Acknowledgements

This work was supported by the International Science & Technology Cooperation Program of Xinjiang Uygur Autonomous Region (no. 20146005), the “Western Light” Program (nos. YBXM 201401 and XBBS 201126) of Chinese Academy of Sciences, the “CAS Action Plan for the Development of Western China” (no. KGZD-EW-502), the National Nature Science Foundation of China (nos. 21173261, 51463008, and 51402134), the “Youth Technology Innovation Talents Culture Engineering” of Tianshan Talent Project of Xinjiang Uygur Autonomous Region of China (no. 2013721045), the CAS/SAFEA International Partnership Program for Creative Research Teams and the CAS “Cross-Cooperation Program for Creative Research Teams”.

Appendix A. Supplementary data

Supplementary data associated with this article can be found, in the online version, at <http://dx.doi.org/10.1016/j.apcatb.2015.07.033>

References

- [1] J. Herney-Ramirez, M.A. Vicente, L.M. Madeira, *Appl. Catal. B: Environ.* 98 (2010) 10–26.
- [2] H. Rong, S. Cai, Z. Niu, Y. Li, *ACS Catal.* 3 (2013) 1560–1563.
- [3] P.H. Howard, D.C. Muir, *Environ. Sci. Technol.* 47 (2013) 5259–5266.
- [4] J.F. Quensen III, S.A. Mueller, M.K. Jain, J.M. Tiedje, *Science* 280 (1998) 722–724.
- [5] G.K. Parshetti, R.A. Doong, *Water Res.* 45 (2011) 4198–4210.
- [6] J. Liu, Y. Wang, Z. Liu, X. Zhang, D.D. Sun, *Adv. Funct. Mater.* 20 (2010) 4175–4181.
- [7] M. Hojaberdiiev, R.M. Prasad, K. Morita, Y. Zhu, M.A. Schiavon, A. Gurlo, R. Riedel, *Appl. Catal. B: Environ.* 115–116 (2012) 303–313.
- [8] S. Liu, J. Yu, M. Jaroniec, *J. Am. Chem. Soc.* 132 (2010) 11914–11916.

- [9] S. Han, L. Hu, N. Gao, A.A. Al-Ghamdi, X. Fang, *Adv. Funct. Mater.* 24 (2014) 3725–3733.
- [10] J. Liu, Y. Liu, N. Liu, Y. Han, X. Zhang, H. Huang, Y. Lifshitz, S. Lee, J. Zhong, Z. Kang, *Science* 347 (2015) 970–974.
- [11] Z. Yi, J. Ye, N. Kikugawa, T. Kako, S. Ouyang, H.S. Williams, H. Yang, J. Cao, W. Luo, Z. Li, Y. Liu, R.L. Withers, *Nat. Mater.* 9 (2010) 559–564.
- [12] F. Bonaccorso, L. Colombo, G. Yu, M. Stoller, V. Tozzini, A.C. Ferrari, R.S. Ruoff, V. Pellegrini, *Science* 347 (2015) 1246501–1246509.
- [13] Y. Qu, X. Duan, *Chem. Soc. Rev.* 42 (2013) 2568–2580.
- [14] L. Li, P.A. Salvador, G.S. Rohrer, *Nanoscale* 6 (2014) 24–42.
- [15] Y. Cui, J. Briscoe, S. Dunn, *Chem. Mater.* 25 (2013) 4215–4223.
- [16] J.H. Haenl, P. Irvin, W. Chang, R. Uecker, P. Reiche, Y.L. Li, S. Choudhury, W. Tian, M.E. Hawley, B. Craig, A.K. Tagantsev, X.Q. Pan, S.K. Streiffer, L.Q. Chen, S.W. Kirchoefer, J. Levy, D.G. Schlom, *Nature* 430 (2004) 758–761.
- [17] L. Yang, S. Luo, Y. Li, Y. Xiao, Q. Kang, Q. Cai, *Environ. Sci. Technol.* 44 (2010) 7641–7646.
- [18] J. Guo, S. Ouyang, P. Li, Y. Zhang, T. Kako, J. Ye, *Appl. Catal. B: Environ.* 134–135 (2013) 286–292.
- [19] M.M. Kuklja, R.V. Tsyshhevsky, O. Sharia, *J. Am. Chem. Soc.* 136 (2014) 13289–13302.
- [20] T. Cao, Y. Li, C. Wang, C. Shao, Y. Liu, *Langmuir* 27 (2011) 2946–2952.
- [21] J. Pan, G. Liu, G.Q. Lu, H.M. Cheng, *Angew. Chem. Int. Ed.* 50 (2011) 2133–2137.
- [22] C.R. Bowen, H.A. Kim, P.M. Weaver, S. Dunn, *Energy Environ. Sci.* 7 (2014) 25–44.
- [23] S. Dunn, P.M. Jones, D.E. Gallardo, *J. Am. Chem. Soc.* 129 (2007) 8724–8728.
- [24] X. Fan, L. Zang, M. Zhang, H. Qiu, Z. Wang, J. Yin, H. Jia, S. Pan, C. Wang, *Chem. Mater.* 26 (2014) 3169–3174.
- [25] X. Chen, S. Shen, L. Guo, S.S. Mao, *Chem. Rev.* 110 (2010) 6503–6570.
- [26] W. Zhang, W. Cheng, H. Zhang, L. Geng, C. Lin, Z. He, *J. Am. Chem. Soc.* 132 (2010) 1508–1509.
- [27] Y. Yang, S. Pan, H. Li, J. Han, Z. Chen, W. Zhao, Z. Zhou, *Inorg. Chem.* 50 (2011) 2415–2419.
- [28] H. Wu, S. Pan, H. Yu, Z. Chen, F. Zhang, *Solid State Sci.* 14 (2012) 936–940.
- [29] X. Chen, C. Yang, X. Chang, H. Zang, W. Xiao, *J. Alloys Compd.* 492 (2010) 543–547.
- [30] X. Chen, M. Li, X. Chang, H. Zang, W. Xiao, *J. Solid State Chem.* 180 (2007) 1658–1663.
- [31] R.T. Sanderson, *J. Inorg. Nucl. Chem.* 25 (1966) 1553–1565.
- [32] D.C. Ghosh, T. Chakraborty, *J. Mol. Struct.* 906 (2009) 87–93.
- [33] I.D. Brown, D. Altermatt, *Acta Crystallogr. B41* (1985) 244–247.
- [34] S. Han, Y. Wang, Q. Jing, H. Wu, S. Pan, Z. Yang, *Dalton Trans.* 44 (2015) 5810–5817.
- [35] X. Ma, B. Lu, D. Li, R. Shi, C. Pan, Y. Zhu, *J. Phys. Chem. C* 115 (2011) 4680–4687.
- [36] W. Melitz, J. Shen, A.C. Kummel, S. Lee, *Surf. Sci. Rep.* 66 (2011) 1–27.
- [37] H.S. Kim, S.K. Kim, B.J. Kim, K.S. Shin, M.K. Gupta, H.S. Jung, S.W. Kim, N.G. Park, *J. Phys. Chem. Lett.* 6 (2015) 1729–1735.
- [38] Z. Lou, B. Huang, Z. Wang, X. Ma, R. Zhang, X. Zhang, X. Qin, Y. Dai, M.H. Whangbo, *Chem. Mater.* 26 (2014) 3873–3875.
- [39] G. Xie, K. Zhang, B. Guo, Q. Liu, L. Fang, J.R. Gong, *Adv. Mater.* 25 (2013) 3820–3839.
- [40] D.S. Shen, X.W. Liu, H.J. Feng, *J. Hazard. Mater.* 119 (2005) 239–243.
- [41] M. Hunger, J. Weitkamp, *Angew. Chem. Int. Ed.* 40 (2001) 2954–2971.